



Anisotropy of Al–Li alloy plate and its heredity effect in mechanical property distribution of spun-dome

Ben LIN^{1,2,3}, Peng-cheng MA⁴, Hao-ran LI⁵, San-xi DENG⁵,
Guang-jun ZENG⁵, Jian-guo TANG⁵, Jin-feng LI⁵, Xi-wu LI^{1,2}

1. State Key Laboratory of Nonferrous Metals and Processes, GRINM Group Co., Ltd., Beijing 100088, China;
2. General Research Institute for Nonferrous Metals, Beijing 100088, China;
3. China Academy of Launch Vehicle Technology, Beijing 100076, China;
4. Aerospace Research Institute of Materials Processing and Technology, Beijing 100076, China;
5. School of Materials Science and Engineering, Central South University, Changsha 410083, China

Received 20 January 2022; accepted 7 June 2022

Abstract: The mechanical properties and grain structures of 2A55 Al–Li alloy plate with 20 mm in thickness after T6-aging at 165 °C for 24 h were investigated. The aging precipitates, grain structures and mechanical property distribution along the circumferential and axial directions in the T6-aged spun-dome with 1 m in diameter spin-deformed through the 2A55 Al–Li alloy plate with 20 mm in thickness were studied. The precipitates in the T6-aged dome include a great number of $T1$ (Al_2CuLi) precipitates and a small number of δ' (Al_3Li) and θ' (Al_2Cu) precipitates. The distribution of $T1$ precipitates is uneven, which is characterized by dense distribution at subgrain boundaries and the formation of precipitate-free zone (PFZ) at high angle grain boundaries. The T6-aged plate possesses almost same strength along a same direction, but there exists anisotropy with the lowest strength along 45° direction and the highest strength along the rolling direction. The T6-aged dome possesses great mechanical property discrepancy along a same circumferential direction and axial direction, which is correlated with the variation of the angle of the dome circumferential direction and axial direction to the rolling direction and the resulting different textures and grain aspect ratio at different locations. There exists a heredity effect in the grain structures and mechanical properties from the original hot-rolled plate to the subsequent spin-deformed dome.

Key words: Al–Li alloy; spin-deformation; anisotropy; mechanical properties; texture

1 Introduction

Al–Li alloys were considered as the most attractive Al alloys in the aircraft and aerospace industries because of their desirable properties, such as low density, high specific strength and elastic modulus, good corrosion resistance, excellent cryogenic properties, and low fatigue crack growth rate [1]. In fact, the third generation Al–Li alloys, such as 2195, 2050, 2099, 2196 and 2197 alloys were successfully used and performed excellently in aircraft and aerospace structures [2,3].

Novel Al–Li alloys were developed and are still in development through adjusting main alloying elements of Cu and Li and micro-alloying elements such as Mg, Ag, Mn and Zn [4]. It was reported that Mg+Ag and Mg+Zn additions greatly enhanced the strength of Al–Li alloys [5,6], the representative alloys include 2195 applied in the space shuttle tank [7,8] and 2099 used in Airbus A380 [2]. A super-high strength Al–Li alloy 2055 was developed by a combined addition of Mg, Ag and Zn [9–12]. According to the alloying effect investigation of micro-alloying elements Mg, Ag and Zn [13] and main alloying elements such as Cu

and Li [14], our research group also invented a novel ultra-high strength Al–Li alloy 2A96 (later registered as 2A55). After T8 aging, the representative ultimate tensile strengths of the sheet with 2 mm in thickness and the plate with 10 mm in thickness are 600 and 630 MPa, respectively [15–17].

Single-piece spin-formed dome manufactured from Al–Li alloy plate has the potential application prospect in fabricating cryogenic propellant tanks in carrier rocket. HALES et al [18,19] joined two 2195 Al–Li alloy plates together to provide a sufficiently wide plate through friction stir welding (FSW) and then fabricated a hemispherical dome with 5 m in diameter through spin-forming technology. Spun-domes with diameters of 1 and 3.35 m were also fabricated in China [20–22]. The invented 2A55 Al–Li alloy is potential in application in cryogenic tanks and can be used to fabricate dome through spinning deformation. It is noted that Al–Li alloys possess in-plane anisotropy (IPA), which are affected by texture and grain shape (aspect ratio) [23–27]. The IPA of 2A55 Al–Li alloy plate may be inherited into its subsequent spin-deformed domes, which can lead to strength discrepancy at different locations in the dome and difficulties in structural design. In order to achieve uniform distribution of mechanical properties in the 2A55 Al–Li alloy spun-dome, it is of great significance to clarify the mechanism of mechanical property distribution and therefore effectively reduce this heredity effect. However, there is little research on this heredity effect. Therefore, the anisotropy of 2A55 Al–Li alloy plate and its dependent mechanical property distribution in subsequent T6-aged spin-formed dome were investigated.

2 Experimental

2.1 Materials and procedures

The hot-rolled 2A55 Al–Li alloy plate with 20 mm in thickness and chemical composition of Al–3.75Cu–1.24Li–0.41Mg–0.37Ag–0.11Zr–0.3Mn (mass fraction, wt.%) was received from Southwest Aluminum (Group) Co., Ltd., China. After annealing, a dome with a diameter of 1 m was then spin-formed at approximately 300 °C through using the Al–Li alloy plate.

Top, middle and bottom parts were cut from

about one quarter of the dome. The top, middle and bottom parts were then divided into 4 blocks, respectively (Fig. 1(a)). For simplicity, different 4 blocks in the top group are represented by T-1, T-2, T-3, and T-4, those in the middle group are represented by M-1, M-2, M-3, and M-4, while those in the bottom group are represented by B-1, B-2, B-3, and B-4. Tensile samples were then cut from the blocks at the center through thickness along the circumferential direction (i.e. parallel to the spinning line) and axial direction (i.e. perpendicular to the spinning line), respectively, as shown in Fig. 1(b). In addition, samples for metallography and texture observation were cut at the locations shown in red color. After solution treatment at 510 °C for 50 min, the samples cut from the dome were quenched in cold water and then aged at 165 °C for 24 h.

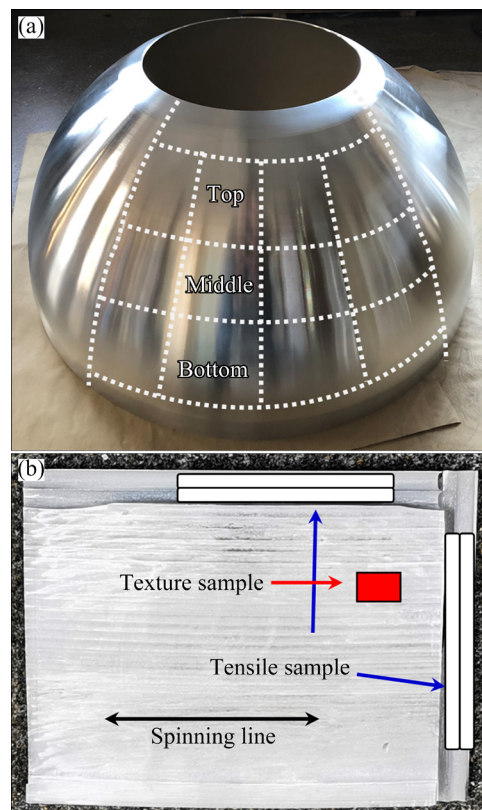


Fig. 1 Milled 2A55 Al–Li alloy dome (a) and schematic diagram of sampling location (b)

For comparison, some samples were cut from the original hot-rolled plate at the center through thickness along the direction with angles of 0°, 30°, 45°, 60°, and 90° to the rolling direction. The samples were then solution-treated and aged at 165 °C for 24 h.

2.2 Tensile tests

After T6 aging, the tensile properties of the samples cut from the plate with 20 mm in thickness and the dome blocks were measured using an MTS 858 universal testing machine with a strain rate of $1.0 \times 10^{-3} \text{ s}^{-1}$ at ambient temperature, respectively. The dimensions of the parallel section in the test samples are 25 mm in length and 5 mm in diameter. Three tensile tests were carried out for each condition, and the average strength and elongation were then calculated.

2.3 Structure observation

The samples for metallographical observations were cut at the center through thickness. The circumferential section parallel to spinning line and axial section perpendicular to spinning line were mechanically grounded and polished, and then anodically treated at room temperature and a voltage of 23 V for 1 min in a solution containing 1.1 g H_3BO_3 , 95 mL H_2O and 3 mL HF. The metallographical observations were performed with an optical microscope (OM, Leica DMI300 M).

The texture detection was carried out through a Bruker D8 Discovery X-ray diffractometer. Incomplete polar figures (IPFs) of $\{111\}$, $\{200\}$ and $\{220\}$ were detected, and the orientation distribution function (ODF) was then calculated. The texture was analyzed quantitatively through particle swarm optimization (PSO). For the texture measurement of the dome sample, the spinning direction was defined as rolling direction.

Precipitates were observed by means of transmission electron microscopy (TEM). The TEM foils were prepared by mechanical grinding and twin-jet electropolishing in a solution containing 30% nitric acid and 70% methanol (volume fraction) at -25°C with a voltage of 15–20 V. TEM observation was performed with a Tecnai G²20 TEM operating at 200 kV through conventional bright-field (BF), dark-field (DF) imaging, and selected area electron diffraction (SAED).

3 Results

3.1 Tensile properties and structures of Al–Li alloy plate

3.1.1 Tensile properties of T6-aged plate

Figure 2 shows the representative tensile curves of the solution-treated and T6-aged Al–Li

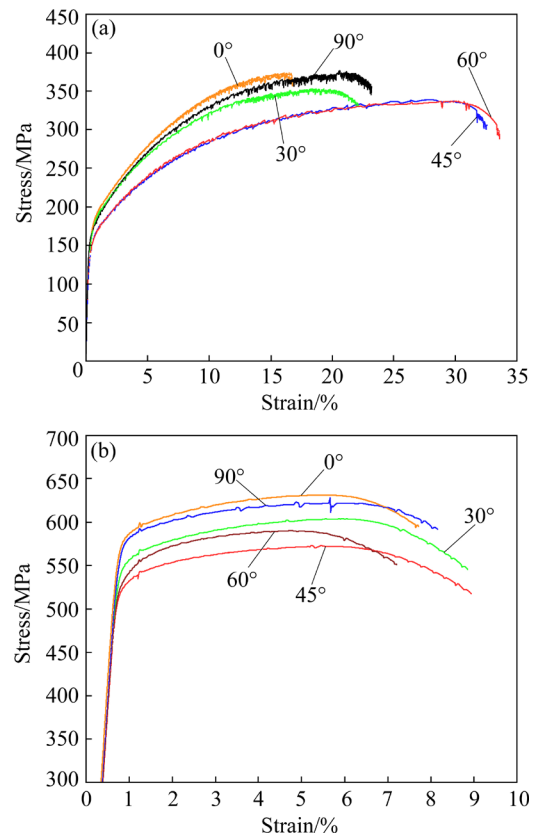


Fig. 2 Representative tensile curves of 2A55 Al–Li alloy plate with 20 mm in thickness along different directions: (a) Solution-treated; (b) T6-aged at 165°C for 24 h

alloy plate along different directions. The solution-treated plate shows different tensile behaviors along different directions. Along the directions with 45° and 60° angles to the rolling direction, the alloy shows lower strength, smaller strain hardening rate and larger elongation than that along the other directions (Fig. 2(a)). After T6 aging, the strain hardening rate along different directions is decreased, but the yield strength difference among different directions is obvious, as shown in Fig. 2(b). The tensile curves also indicate the strength along 45° direction is the lowest and that along the rolling direction is the highest. According to these tensile curves, the yield strength (YS), ultimate tensile strength (UTS) and elongation (EL) after fracture are obtained, as shown in Fig. 3. Both the solution-treated and T6-aged plates possess IPA. However, it should be emphasized that the tensile properties along the same direction are almost the same in both the solution-treated and T6-aged plates, as indicated by the error bar in Fig. 3.

According to Ref. [25], the IPA can be defined as the following equation:

$$IPA = \frac{(N-1)(X_{\max} - X_{\text{mid}1} - X_{\text{mid}2} - \dots - X_{\min})}{(N-1)X_{\max}} \times 100\% \quad (1)$$

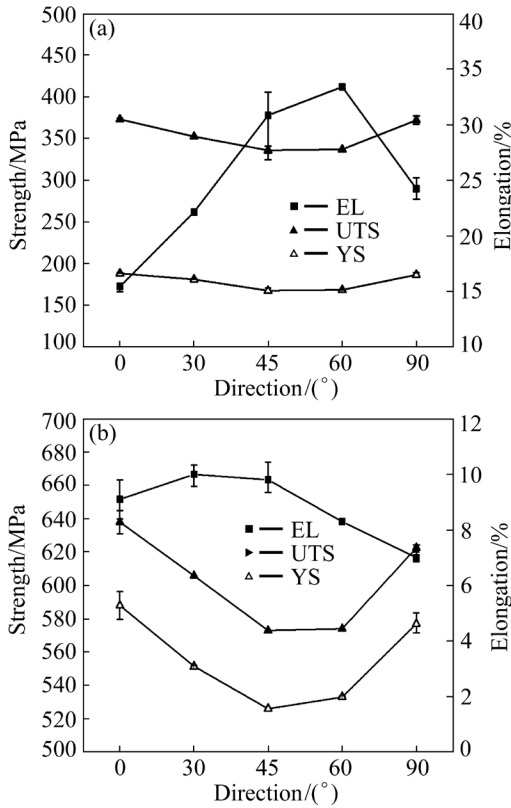


Fig. 3 YS, UTS and EL of 2A55 Al–Li alloy plate along different directions: (a) Solution-treated; (b) T6-aged at 165 °C for 24 h

where $N(=5)$ is the number of stress loading directions, X_{\max} , X_{\min} , and X_{mid} represent the maximum, minimum and intermediate values in the tensile properties along N directions, respectively. The tensile property X can be YS, UTS and EL. Table 1 shows the calculated IPA of YS, UTS and EL. The IPAs of YS and UTS in the solution-treated and T6-aged plates are similar, but the IPA of EL in the solution-treated plate is much higher.

3.1.2 Grain structures of plate

Figure 4 shows the metallographic images of center layer in the solution-treated plate through thickness. The solution-treated plate exhibits pancake shape grains elongated along the rolling direction. It is noted that the aspect ratio on longitudinal section (Fig. 4(a)) is much higher than that on transversal section (Fig. 4(b)).

The ODFs of the center layer in the solution-treated plate with 20 mm in thickness are shown in Fig. 5. There exists obvious Brass texture. The

Table 1 IPAs of YS, UTS and EL in solution-treated and T6-aged 2A55 Al–Li alloy plates (%)

State	YS	UTS	EL
Solution-treated	6.54	6.37	30.76
T6-aged	7.01	6.97	17.8

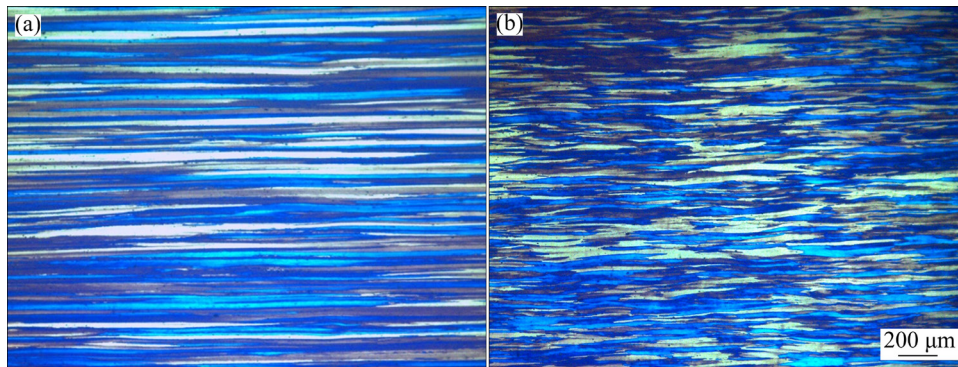


Fig. 4 Metallographic images of center layer in solution-treated plate through thickness on longitudinal section (a) and transversal section (b)

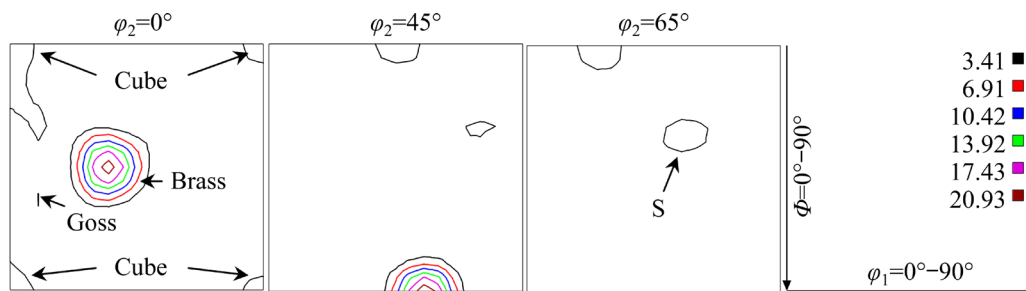


Fig. 5 ODFs of center layer in solution-treated plate with 20 mm in thickness

deformation texture of S component and recrystallization texture of Cube and Goss components can also be found. The volume fraction of the Brass texture and S texture is up to 35% and 16%, respectively, as shown in Table 2.

Table 2 Volume fractions of different textures of center layer in solution-treated plate (vol.%)

Brass	S	Goss	Cube	Total
35.23	16.15	3.91	7.93	63.22

3.2 Tensile properties and structures of Al–Li alloy dome

3.2.1 Tensile properties of T6-aged Al–Li alloy dome

Figure 6 shows the tensile curves of 4 blocks of the bottom group in the Al–Li alloy dome along circumferential direction and axial direction after solution treatment and T6-aging. The tensile curves of different blocks along the same circumferential direction and axial direction are different. Table 3

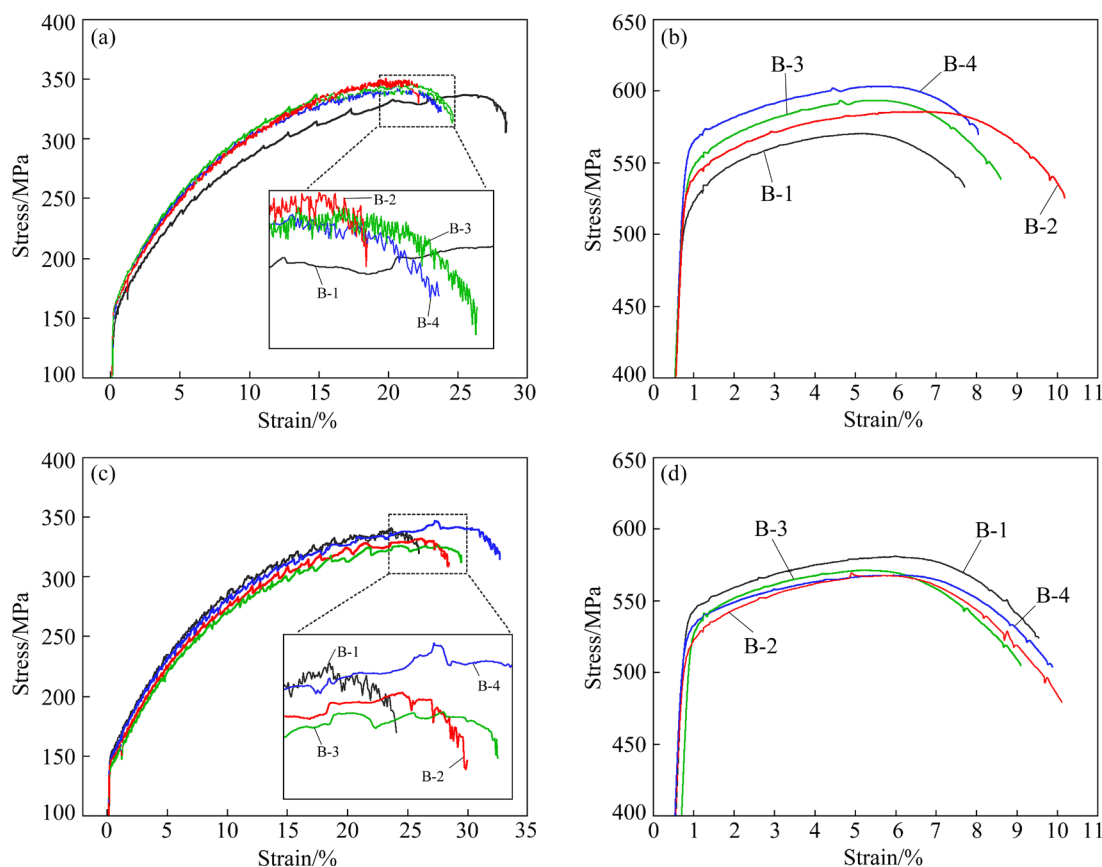


Fig. 6 Tensile curves of 4 blocks in solution-treated and T6-aged bottom group along circumferential direction (a, b) and axial direction (c, d): (a, c) Solution-treated; (b, d) T6-aged

Table 3 Average tensile properties of different blocks in bottom group

Block No.	State	Circumferential direction			Axial direction		
		YS/MPa	UTS/MPa	EL/%	YS/MPa	UTS/MPa	EL/%
B-1	Solution-treated	168.8	336.9	30.5	167.2	334.9	24.1
	T6-aged	519.5	570.0	11.2	541.3	580.0	11.4
B-2	Solution-treated	173.6	345.5	22.7	166.2	332.2	27.3
	T6-aged	537.4	585.0	12.0	519.4	567.0	15.4
B-3	Solution-treated	170.7	341.0	25.0	166.8	328.7	31.2
	T6-aged	543.0	593.0	9.0	531.4	571.0	10.3
B-4	Solution-treated	172.2	347.6	23.6	173.2	343.9	32.3
	T6-aged	561.7	603.0	8.4	528.8	568.0	11.3

shows the specific tensile properties of 4 blocks in the bottom group, and there exists great discrepancy in the strength and elongation. This discrepancy is not caused by accidental error, because the strength of three samples at the same location and along the same direction is almost the same.

3.2.2 Grain structures of dome at different locations

Figure 7 shows the metallographic images of

different blocks in the bottom group on circumferential section and axial section at the center through thickness. For Block B-4, the grains display the elongated morphology along both circumferential direction and axial direction, but the aspect ratio along the circumferential direction is higher (Figs. 7(a, b)). For Block B-3, the grains display similar feature (Figs. 7(c, d)).

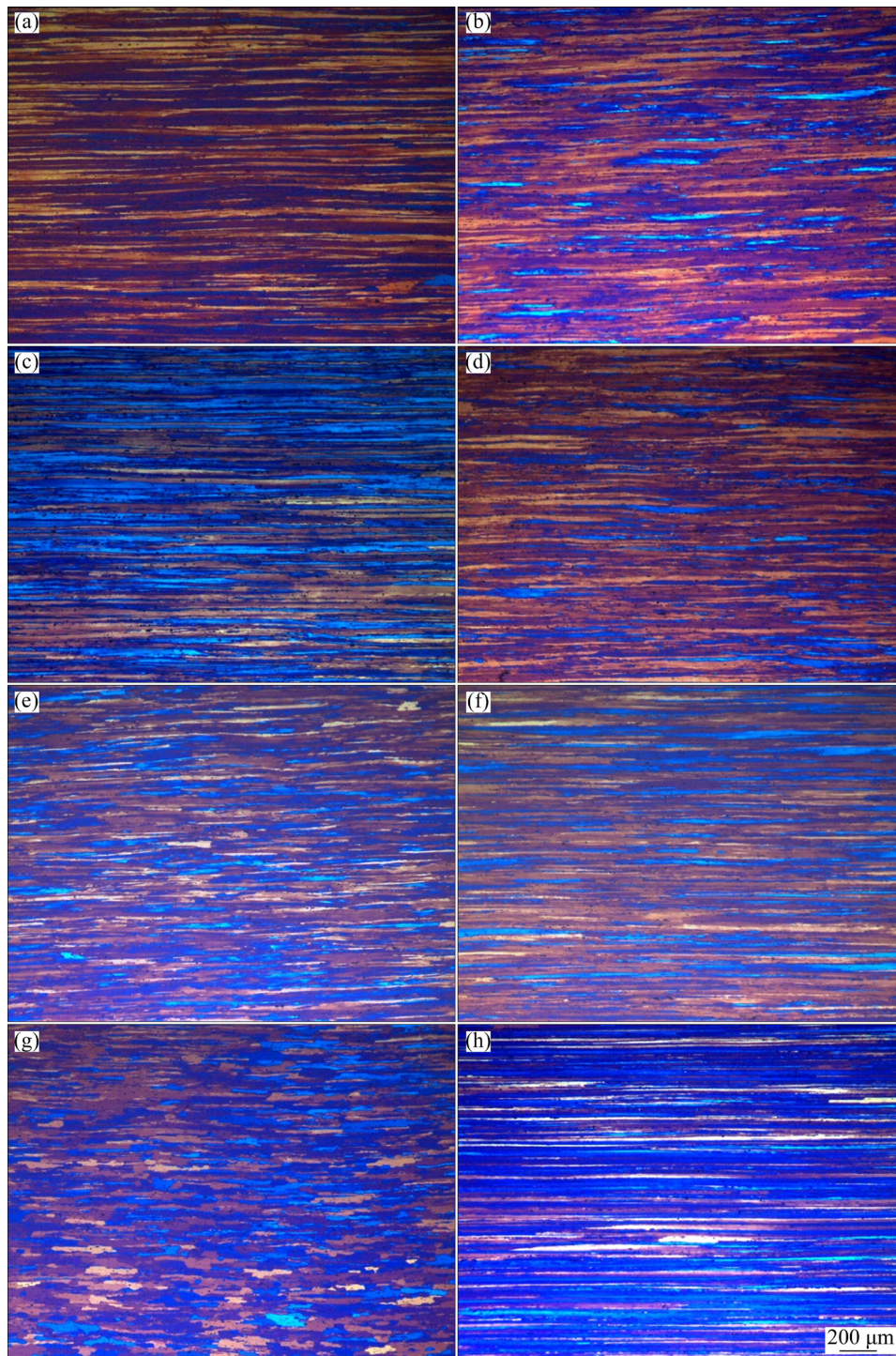


Fig. 7 Metallographic images of different solutionized dome blocks in bottom group along circumferential direction (a, c, e, g) and axial direction (b, d, f, h) at center through thickness: (a, b) B-4; (c, d) B-3; (e, f) B-2; (g, h) B-1

For Block B-2, there is no significant difference between the aspect ratio on the circumferential section and the axial section (Figs. 7(e, f)). However, for Block B-1, the grain morphology is much different, and the aspect ratio on the circumferential section is much lower than that on the axial section (Figs. 7(g, h)).

Figure 8 shows the ODFs of different solution-treated dome blocks in the bottom group at the center through thickness, which indicates that the texture types are much different. In Blocks B-4 and B-3, there exist obvious deformation textures of Brass, Cu and S components (Figs. 8(a, b)). However, in Blocks B-2 and B-1, the deformation

textures weaken or disappear (Figs. 8(c, d)). Table 4 shows the volume fractions of different textures in the solution-treated blocks of the bottom group. The deformation texture volume fraction in Blocks B-3 and B-4 is much higher than that in Blocks B-1 and B-2. However, it is also noted that the volume fraction of deformation textures in solution-treated Blocks B-3 and B-4 is obviously lower than that in the original solution-treated plate.

3.2.3 Precipitates in T6-aged dome block

Figure 9 shows the SAED patterns and TEM images of the dome after T6 aging at 165 °C for 24 h. In the $[100]_{Al}$ SAED pattern, spots at $\{110\}_{Al}$ and $\{100\}_{Al}$ are observed. In addition, weak and

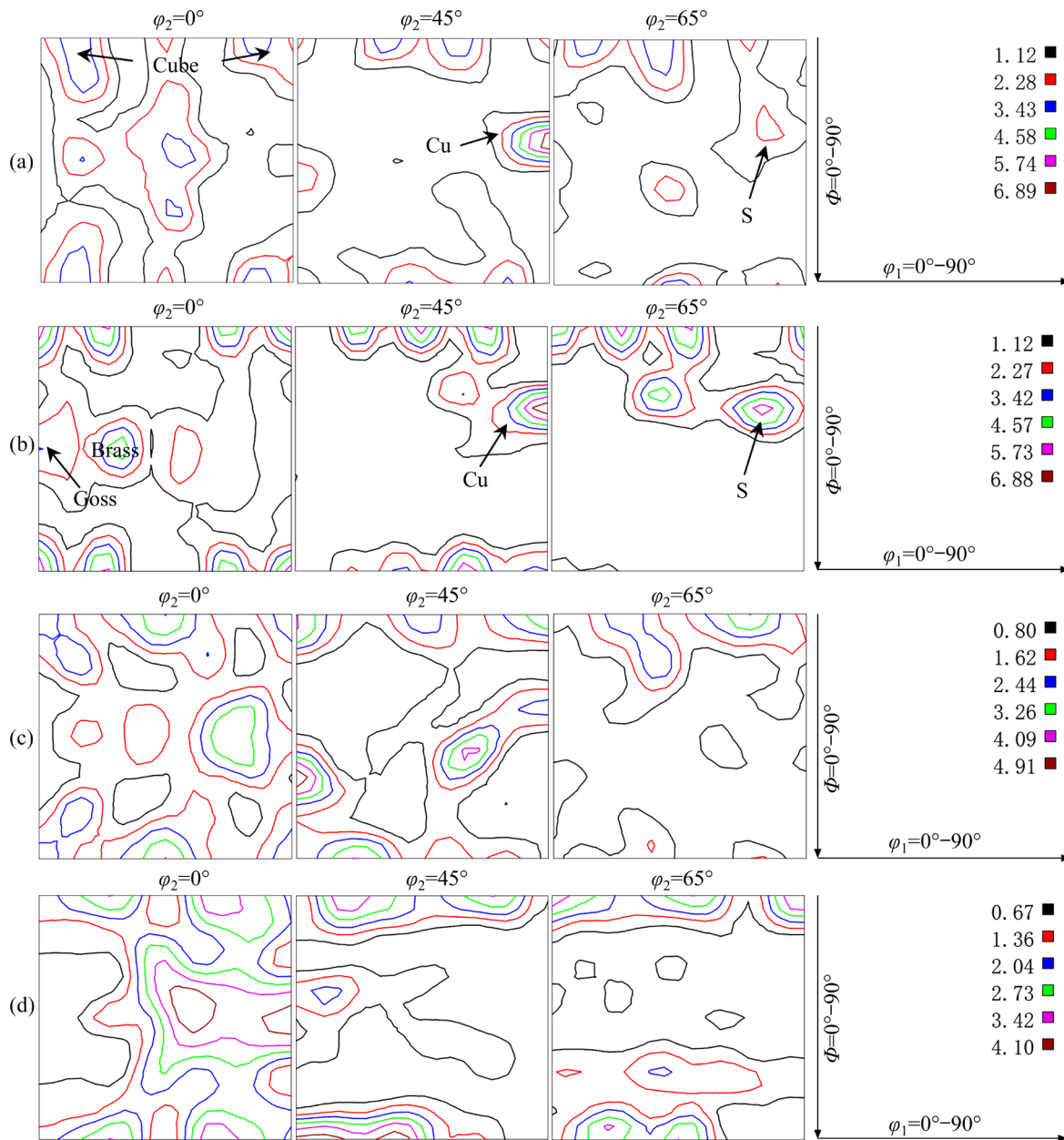
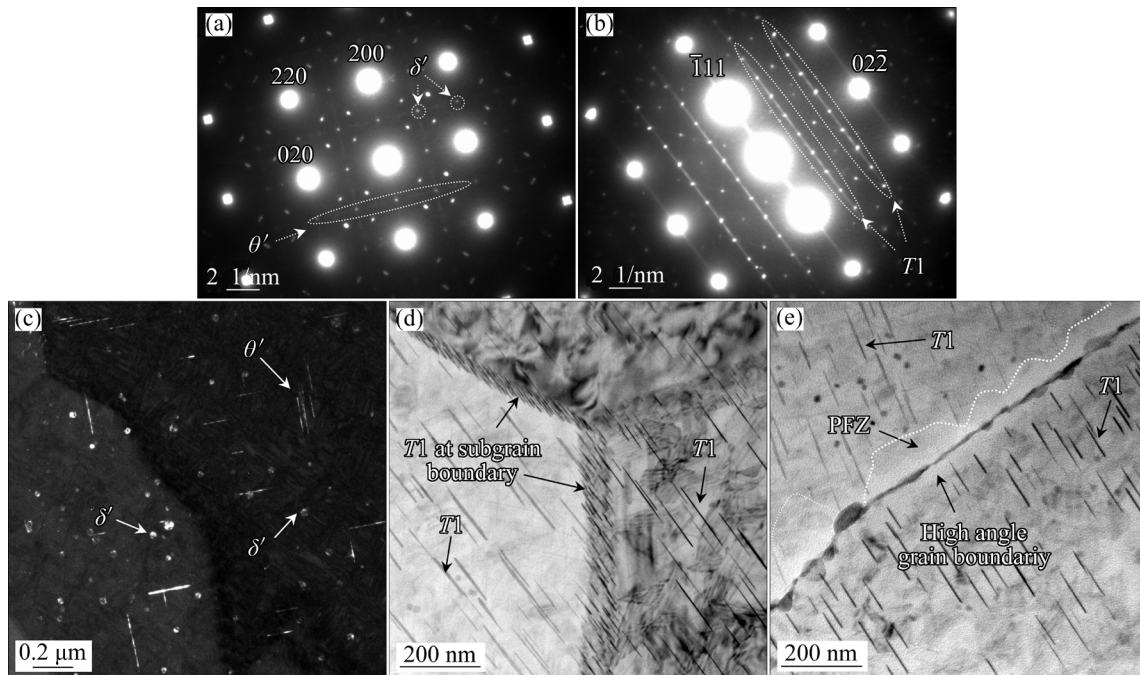


Fig. 8 ODFs of different solution-treated dome blocks in bottom group: (a) Block B-4; (b) Block B-3; (c) Block B-2; (d) Block B-1

Table 4 Volume fractions of different textures in solution-treated blocks in bottom group at center through thickness (vol.%)

Block No.	Brass	Cu	S	Cube	Goss	R-Cube	(101)[$\bar{1}\bar{1}\bar{1}$]	Deformation texture	Total
B-1	14.02	0	0	8.45	0	2.45	21.36	14.02	46.28
B-2	5.8	5.78	0	7.57	0	8.19	0	10.58	27.34
B-3	11.31	9.69	14.53	10.87	4.11	0	0	35.53	50.51
B-4	16.78	12.85	8.38	11.43	7.25	0	0	38.01	56.69

**Fig. 9** SAED patterns and TEM images of dome after T6 aging at 165 °C for 24 h: (a) $[100]_{\text{Al}}$ SAED pattern; (b) $[112]_{\text{Al}}$ SAED pattern; (c) DF image showing δ' and θ' precipitates viewed along $\langle 100 \rangle_{\text{Al}}$ direction; (d, e) BF images showing $T1$ precipitates viewed along $\langle 112 \rangle_{\text{Al}}$ direction

discontinuous streaks passing through $\{110\}_{\text{Al}}$ spots are distinguished (Fig. 9(a)). Accordingly, a small number of δ' (Al_3Li) precipitates and θ' (Al_2Cu) precipitates are observed in the DF image viewed along $\langle 100 \rangle_{\text{Al}}$ direction (Fig. 9(c)). In the $[112]_{\text{Al}}$ SAED pattern, bright streaks passing through $1/3\{220\}_{\text{Al}}$ and $2/3\{220\}_{\text{Al}}$ (Fig. 9(b)) are observed, indicating a great number of $T1$ precipitates. Accordingly, a great number of $T1$ precipitates are observed in the BF images viewed along $\langle 112 \rangle_{\text{Al}}$ direction (Figs. 9(d, e)). However, $T1$ precipitates are distributed unevenly, and their number density at subgrain boundaries is much higher than that within the grain (Fig. 9(d)). At the high angle grain boundaries, the $T1$ precipitates are scarce and a PFZ (precipitate-free zone) is formed (Fig. 9(e)).

The above TEM observations indicate that the precipitates of 2195 Al–Li alloy dome with T6

aging at 165 °C for 24 h include $T1$, θ' and δ' . The main precipitates are $T1$, which are distributed unevenly.

4 Discussion

4.1 In-plane anisotropy of Al–Li alloy plate

Both the solution-treated and T6-aged Al–Li alloy plates with 20 mm in thickness possess IPA, which is related to the texture existing in the plate. The plate was fabricated through hot-rolling, during which dynamic recovery and dynamic recrystallization occurred and the stored energy was released. During the subsequent solution treatment, the stored energy is too low to activate the recrystallization. Deformation textures with a large volume fraction were therefore maintained in the solution-treated plate and the grains kept as

thin-pancake shape.

The IPA of the solution-treated and T6-aged Al–Li alloy plates is correlated with Schmid factor (f_{SF}) along different directions caused by the deformation textures. The f_{SF} value is defined as

$$f_{SF,i} = \cos \varphi_i \cos \lambda_i \quad (2)$$

where φ_i is the angle between tensile direction and normal direction of the i th slip system, and λ_i is the angle between tensile direction and slip direction of the i th slip system. With the f_{SF} , the resolved shear stress τ_i on the i th slip system due to external tensile stress σ can be calculated as

$$\tau_i = \sigma f_{SF,i} \quad (3)$$

As $\tau_i \leq \tau_c$ (τ_c is the critical resolved shear stress), the slip system with maximum f_{SF} value is the most possible slip system activated during tensile deformation. Along different directions, the maximum f_{SF} for a certain texture component is different. Therefore, the total f_{SF} ($f_{SF,T}$) for the solution-treated plate along different directions can therefore be calculated. Considering the specific f_{SF} values of different textures and the average f_{SF} (0.33) of texture-free FCC polycrystal [28], the $f_{SF,T}$ is calculated according to the following equation:

$$f_{SF,T} = \sum_{i=0}^n f_{SF,i} \cdot F_i + f_{SF,0} \cdot F_0 \quad (4)$$

where F_i means the fraction of different textures, i describes the texture type and n refers to the number of textures in the sample. $f_{SF,0}$ and F_0 represent the average f_{SF} and fraction of the rest texture-free polycrystal without texture, respectively.

The maximum f_{SF} values of different textures in Al alloys along 0° , 45° and 90° directions are presented in Table 5. The $f_{SF,T}$ values for the solution-treated plate along these directions are

Table 5 Maximum f_{SF} of different textures and $f_{SF,T}$ along 0° , 45° and 90° directions for solution-treated plate

Texture type	Volume fraction / %	Maximum f_{SF}		
		0°	45°	90°
Brass	35.23	0.4096	0.4453	0.2753
Cu	0	0.2753	0.5	0.4082
S	16.15	0.4254	0.4819	0.4449
Cube	7.93	0.4082	0.4082	0.4082
Goss	3.91	0.4082	0.3485	0.4048
$f_{SF,T}$		0.3827	0.4021	0.3384

therefore calculated according to Eq. (4). Because the low temperature aging has little influence on the texture [23], the texture can be assumed to be the same for the T6-aged and solution-treated plates. The $f_{SF,T}$ values of the T6-aged plate are therefore almost the same to those of the solution-treated plate.

It is found that the $f_{SF,T}$ of the sample along 45° direction is higher than that of the sample along both 0° and 90° directions. Higher $f_{SF,T}$ means easier sliding of dislocations and lower YS. The highest $f_{SF,T}$ of the sample along 45° direction contributes to its lowest strength. However, it is noted that the sample along 90° direction possesses the lowest $f_{SF,T}$, but its strength is not the lowest.

Another factor should be considered. Along the 90° direction, the maximum f_{SF} of Brass texture (0.2753) is much lower, and that of S texture (0.4449) is obviously higher than that of other textures. At the beginning of the tensile deformation, S texture with maximum f_{SF} of 0.4449 should be quickly activated. Therefore, although the total $f_{SF,T}$ is lower, the strength along 90° direction is still a little lower than that along 0° direction.

4.2 Mechanical property distribution within Al–Li alloy dome

The strengths along both the circumferential direction and axial direction in different blocks are different (Fig. 6), which are associated with grain structure difference at different locations. It is noted that the grain morphologies of different blocks in the bottom group along the circumferential direction and axial direction are different, which is characterized by various grain aspect ratios and texture types and volume fractions.

It is known that f_{SF} difference causes strength discrepancy, and higher f_{SF} corresponds to lower YS. According to Eq. (4), combined with the maximum f_{SF} along 0° direction (corresponding to circumferential direction in the dome) and 90° direction (corresponding to axial direction in the dome) shown in Table 5, the $f_{SF,T}$ along the circumferential direction and axial direction in different blocks can be calculated when total texture component and texture-free component are included, as shown in Table 6. However, the calculated results are inconsistent with the performance relationship that higher $f_{SF,T}$ corresponds to lower YS. For example, along the circumferential direction, according to its almost the lowest $f_{SF,T}$ (0.3438), Block

Table 6 $f_{SF,T}$ and YS values of blocks in bottom group along 0° and 90° directions

Block No.	Direction	$f_{SF,T}$		Average YS of ST/MPa	EL of ST / %	Average YS of T6/MPa	EL of T6/%
		Total included	Components excluded*				
B-1	0°	0.3664	0.3664	169	30.9	519	11.2
	90°	0.3476	0.3090	172	24.6	537	11.4
B-2	0°	0.3438	0.3279	174	21.9	537	12.0
	90°	0.3437	0.3277	168	26.2	519	15.4
B-3	0°	0.3592	0.3326	172	24.2	543	9.0
	90°	0.3598	0.3287	164	30.5	531	10.2
B-4	0°	0.3589	0.3236	172	22.9	561	8.4
	90°	0.3551	0.3089	174	32.5	528	11.3

ST: Solution-treated; * Along circumferential and axial directions, the Cu component and Brass component are excluded, respectively

B-2 should possess almost the highest YS. However, its YS is actually lower than that of Blocks B-3 and B-4 along the circumferential direction.

It should be noted that Cu texture along 0° direction and Brass texture along 90° direction have the maximum f_{SF} of 0.2753, thus the corresponding sliding system actually cannot be activated as the alloy begins to yield due to its too low f_{SF} . Based on this analysis, the $f_{SF,T}$ calculation along 0° direction and 90° direction should exclude the Cu or Brass components, respectively. The $f_{SF,T}$ is therefore re-calculated, as shown in Table 6.

According to Table 6, the $f_{SF,T}$ of different blocks in the bottom group along circumferential direction changes in the following order: $f_{SF,T,B-4} < f_{SF,T,B-2} < f_{SF,T,B-3} < f_{SF,T,B-1}$. This sequence corresponds to the lowest strength of Block B-1 and the highest strength of Block B-4 along the circumferential direction. In addition, the volume fraction of Cu texture displays as B-4>B-3>B-2>B-1. Along the circumferential direction (0° direction), the maximum f_{SF} (0.2753) of Cu texture is much lower than that of the other texture components, the corresponding grains are unable to deform and also impede the deformation of neighboring grains due to coordinated deformation, which therefore leads to greater deformation resistance during the tensile process. As a result, the YS of Block B-3 is higher than that of Block B-2 along the circumferential direction.

Along the axial direction, the $f_{SF,T}$ of different blocks are as follows: $f_{SF,T,B-4} \approx f_{SF,T,B-1} < f_{SF,T,B-2} \approx f_{SF,T,B-3}$. In addition, along the 90° direction (i.e. axial direction), Brass texture has a much lower maximum f_{SF} , but S texture has a maximum f_{SF}

obviously higher than the other textures. Blocks B-1, B-3 and B-4 have higher volume fractions of Brass texture than Block B-2, and Block B-3 has the highest volume fraction of S texture. These factors therefore result in that the YS of Block B-2 is lower than those of Blocks B-1, B-3 and B-4 in the bottom group along the axial direction.

4.3 Relevance of plate in-plane anisotropy and mechanical property distribution within dome

The mechanical properties of the T6-aged plate along the same direction are almost the same, but they are different along different directions. As discussed above, this in-plane anisotropy of the T6-aged plate with 20 mm in thickness is correlated with its non-recrystallization and the existence of the deformation texture.

The mechanical properties of the dome block with T6-aging along the same direction are much different. The measured YS of 4 dome blocks in the bottom group along the same circumferential direction changes from 519 to 561 MPa, while it changes from 519 to 541 MPa along the same axial direction. This mechanical property distribution in the spun-dome is different from the characteristics of almost the same strength along the same direction in the plate. Although the mechanical property distribution in the dome is dependent on grain structures, i.e. the different textures at different locations, there exists correlation between the mechanical property distribution in the dome and that in the plate.

The dome was spun through a circular hot-rolled plate after annealing. At different locations, the angle between the spinning direction

and the original rolling direction of the plate changes during the spinning process. As a result, the angles between the circumferential (or axial) direction of the dome and the rolling direction of the plate are different at different locations. As shown in Fig. 10, the circumferential direction to the original rolling direction at Points *A*, *B* and *C* is much different, of which the angles are 0° , 45° and 90° , respectively. The directions of *OD*, *OE*, and *OF* are all the axial directions, but their angles to the rolling direction are 90° , 45° and 0° , respectively. This leads to a feature that the grain structures (grain aspect ratio and textures) at different locations are different (Fig. 7 and Fig. 8). There hence exists a mechanical property discrepancy along the same circumferential or axial direction in the bottom group of the dome (Table 3). Actually, due to the same reason, this property discrepancy also exists in the middle and bottom groups, as shown in Fig. 11.

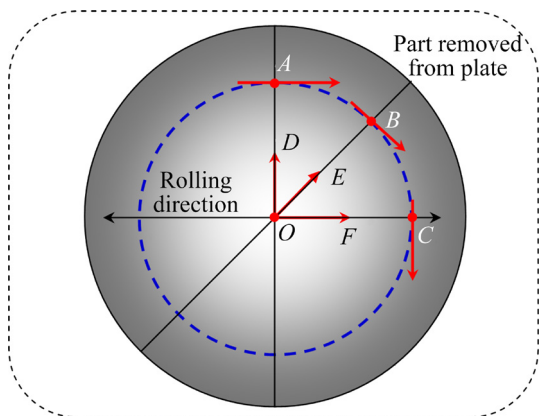


Fig. 10 Schematic diagram of circumferential and axial directions to original rolling direction

The above analysis indicates there exists a heredity effect in the grain structures and mechanical properties from the original hot-rolled plate to the subsequent spin-deformed dome. For effective application in the spun-dome of rocket tank, the above property discrepancy of 2A55 Al–Li alloy along the same direction should be abated, therefore, it is important to eliminate or weaken this heredity effect by controlling the grain structures (grain aspect ratio and textures) through adjusting the spinning process parameters. In addition, comprehensive understanding the mechanical property distribution of the dome is also critical for the design of spun Al–Li alloy dome. These two aspects should be further studied thoroughly.

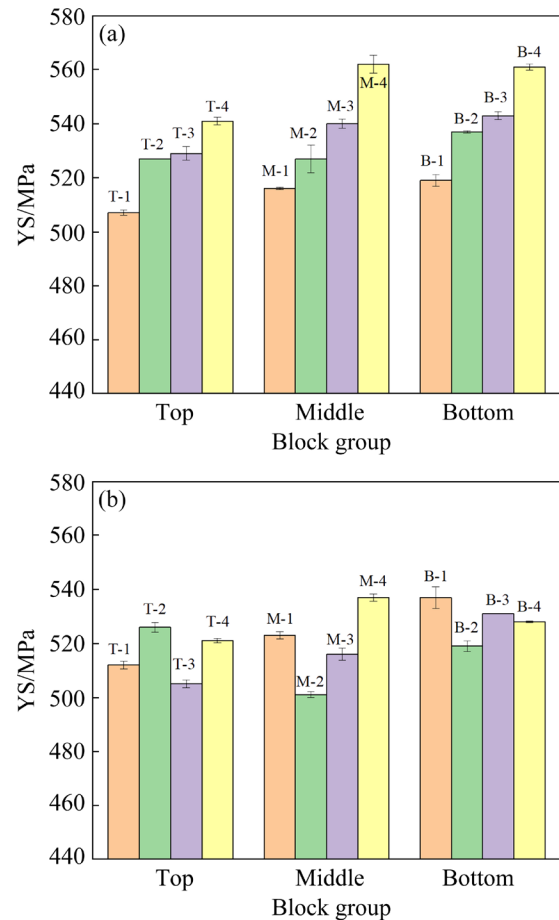


Fig. 11 Average YS distribution at different groups along circumferential (a) and axial (b) directions

5 Conclusions

(1) The precipitates in the spun 2A55 Al–Li alloy dome after T6 aging at 165°C for 24 h include a great number of *T1* precipitates and a small number of δ' and θ' precipitates. *T1* precipitates are distributed unevenly, their number density at subgrain boundaries is much higher than that within the grain, and PFZs are formed at high angle grain boundaries.

(2) The plate with 20 mm in thickness possesses almost the same strength along the same direction, but there exists the anisotropy with the lowest strength along 45° direction and the highest strength along the rolling direction. This anisotropy is caused by a great number of deformation textures (Brass and S components) with a volume fraction of about 51% after solution treatment.

(3) The spun-dome fabricated through the rolled plate possesses great strength discrepancy along the same circumferential direction and axial direction, which is correlated with its different grain

aspect ratios and textures at different locations.

(4) There exists a heredity effect in the grain structures and mechanical properties from the original hot-rolled plate to the subsequent spin-deformed dome. It is critical to comprehensively understand the strength discrepancy along the same direction caused by this heredity effect and eliminate or weaken this heredity effect by controlling the grain structures.

References

- [1] RIOJA R J, LIU J. The evolution of Al–Li base products for aerospace and space applications [J]. *Metallurgical and Materials Transactions A*, 2012, 43: 3325–3337.
- [2] RAJAN R, KAH P, MVOLA B, MARTIKAINEN J. Trends in aluminium alloy development and their joining methods [J]. *Reviews on Advanced Materials Science*, 2016, 44(4): 383–397.
- [3] RIOJA R J, DENZER D K, MOOY D, VENEMA G. Lighter and stiffer materials for use in space vehicles [C]//WEILAN H, ROLLETT A, CASSADA W A. *Proceedings of the 13th International Conference on Aluminum Alloys (ICAA13)*. Pittsburgh: A John Wiley & Sons, Inc., 2012: 593–598.
- [4] LI Jin-feng, NING hong, LIU Dan-yang, ZHENG Zi-qiao. Alloying and micro-alloying in Al–Cu–Li series alloys [J]. *The Chinese Journal of Nonferrous Metals*, 2021, 31(2): 258–279. (in Chinese)
- [5] WEI Xiu-yu, ZHENG Zi-qiao, SHE Ling-juan, CHEN Qiu-ni, LI Shi-chen. Micro-alloying roles of Mg and Zn additions in 2099 Al–Li alloy [J]. *Rare Metal Materials and Engineering*, 2010, 39(9): 1583–1587. (in Chinese)
- [6] ITOH G, CUI Q, KANNO M. Effects of a small addition of magnesium and silver on the precipitation of η phase in an Al–4%–1.1%Li–0.2%Zr alloy [J]. *Materials Science Engineering A*, 1996, 211: 128–37.
- [7] CHEN P S, KURUVILLA A K, MALONE T W, STANTON W P. The effects of artificial aging on the microstructure and fracture toughness of Al–Cu–Li alloy 2195 [J]. *Journal of Materials Engineering and Performance*, 1998, 7(5): 682–690.
- [8] LEQUEU P, SMITH K P, DANIELOU A. Aluminum–copper–lithium alloy 2050 developed for medium to thick plate [J]. *Journal of Materials Engineering and Performance*, 2010, 19(6): 841–847.
- [9] BODILY B, HEINIMANN M, BRAY G, COLVIN E, WITTERS J. Advanced aluminum solutions for next-gen aerospace structures [J]. *Aerospace Engineering*, 2013, 2: 34–37.
- [10] BALDUCCI E, CESCHINI L, MESSIERI S. High temperature tensile tests of the lightweight 2099 and 2055 Al–Cu–Li alloy: A comparison [J]. *JOM*, 2018, 70 (11): 2716–2725.
- [11] BALDUCCI E, CESCHINI L, MESSIERI S, WENNER S, HOLMESTAD R. Effects of overaging on microstructure and tensile properties of the 2055 Al–Cu–Li–Ag alloy [J]. *Materials Science and Engineering A*, 2017, 707: 221–231.
- [12] JAMBOR M, NOVY F, BOKUVKA O, TRSKO L. The natural aging behavior of the AA2055 Al–Cu–Li alloy [J]. *Transportation Research Procedia*, 2019, 40: 42–45.
- [13] LUO Xian-fu, ZHENG Zi-qiao, ZONG Ji-fa, ZHANG Hai-feng, ZHONG Jing, LI Shi-chen, LI Jin-feng. Effects of Mg, Ag and Zn multi-alloying on aging behavior of new Al–Cu–Li alloy [J]. *The Chinese Journal of Nonferrous Metals*, 2013, 23: 1833–1842. (in Chinese)
- [14] LI Jin-feng, LIU Ping-li, CHEN Yong-lai, ZHANG Xu-hu, ZHENG Zi-qiao. Mechanical properties and microstructures of Mg, Ag and Zn multi-microalloyed Al–(3.2–3.8)Cu–(1.0–1.4)Li alloys [J]. *Transactions of Nonferrous Metals Society of China*, 2015, 25(7): 2103–2112.
- [15] LI Jin-feng, CHEN Yong-lai, ZHANG Xu-hu, LIU Qing, ZHENG Zi-qiao, YAO Yong, WANG Jian. Structures and mechanical properties of a super-high strength Al–Li alloy [J]. *Rare Metal Materials and Engineering*, 2017, 46(12): 3715–3720. (in Chinese)
- [16] WANG Jie-xia, LIU Qing, LI Jin-feng, CHEN Yong-lai, ZHANG Xu-hu, ZHENG Zi-qiao. Effect of aging treatment on the mechanical properties and microstructures of a novel super-high strength Al–Cu–Li–X alloy [J]. *Journal of Central South University (Science and Technology)*, 2018, 49(4): 794–801. (in Chinese)
- [17] LI Jin-feng, CHEN Yong-lai, ZHANG Xu-hu, ZHANG Jian, ZHENG Zi-qiao. Aging behavior and microstructure of a new super-high strength Al–Li alloy sheet [J]. *Aerospace Materials and Technology*, 2016, 46(5): 62–67. (in Chinese)
- [18] HALES S J, TAYON W A. Heat treatment of a friction-stir-welded and spin-formed Al–Li alloy [J]. *Procedia Engineering*, 2011, 10: 2496–2501.
- [19] TAYON W A, DOMACK M S, HALES S J. Correlation of fracture behavior with microstructure in friction stir welded, and spin-formed Al–Li 2195 domes[C]//WEILAN H, ROLLETT A, CASSADA W A. *Proceedings of the 13th International Conference on Aluminum Alloys (ICAA13)*. Pittsburgh: John Wiley & Sons, Inc., 2012: 623–628.
- [20] CHEN Yong-lai, WEN Tao, ZHU Hong-wei, XU Xiu-zhi, MA Peng-cheng, HUANG Si-yuan, DU Zhi-hui. Study on microstructure and mechanical properties of 2195 Al–Li hemispherical shell formed by spinning [J]. *Aerospace Manufacturing Technology*, 2019(1): 17–21. (in Chinese)
- [21] WEN Tao, CHEN Yong-lai, DU Yue, YIN Jia-ming, MA Peng-cheng. Effect of spinning deformation on microstructure and mechanical properties in 2195 Al–Li alloy [J]. *Manned Spaceflight*, 2020, 26(2): 717–722. (in Chinese)
- [22] LI Jin-feng, CHEN Yong-lai, MA Yun-long, ZHANG Xu-hu. Basic research and application technology development of Al–Li alloy in China [J]. *Aerospace Materials and Technology*, 2021, 51(4): 37–47. (in Chinese)
- [23] ZHAO T Z, JIN L, XU Y, ZHANG S H. Anisotropic yielding stress of 2198 Al–Li alloy sheet and mechanisms [J]. *Materials Science and Engineering A*, 2020, 771: 138572.
- [24] BOIS-BROCHU A, BLAIS C, GOMA F A T, LAROUCHE D, BOSELLI J, BROCHU M. Characterization of Al–Li 2099 extrusions and the influence of fiber texture on the anisotropy of static mechanical properties [J]. *Materials Science and Engineering A*, 2014, 597: 62–69.

- [25] XU X, HAO M, CHEN J, HE W, LI G, JIAO C, BURNETT T L, ZHOU X. Influence of microstructural and crystallographic inhomogeneity on tensile anisotropy in thick-section Al–Li–Cu–Mg plates [J]. *Materials Science and Engineering A*, 2022, 829: 142135.
- [26] MISHRA S, SURESH M, MORE A M, BISHT A, NAYAN N, SUWAS S. Texture control to reduce yield strength anisotropy in the third generation aluminum–copper–lithium alloy: Experiments and modeling [J]. *Materials Science and Engineering A*, 2021, 799: 140047.
- [27] CHO K K, CHUNG Y H, LEE C W, KWUN S I, SHIN M C. Effects of grain shape and texture on the yield strength anisotropy of Al–Li alloy sheet [J]. *Scripta Materialia*, 1999, 40(6): 651–657.
- [28] MA Yun-long, LI Jin-feng, ZHANG Run-zhe, TANG Jian-guo, HUANG Cheng, LI Hong-ying, ZHENG Zi-qiao. Strength and structure variation of 2195 Al–Li alloy caused by different deformation processes of hot extrusion and cold-rolling [J]. *Transactions of Nonferrous Metals Society of China*, 2020, 30(4): 835–849.

铝锂合金板材的各向异性及其在旋压壳体力学性能分布中的遗传效应

林 奔^{1,2,3}, 马鹏程⁴, 李昊然⁵, 邓三喜⁵, 曾广俊⁵, 唐建国⁵, 李劲风⁵, 李锡武^{1,2}

1. 有研科技集团有限公司 有色金属材料制备加工国家重点实验室, 北京 100088;
2. 北京有色金属研究总院, 北京 100088;
3. 中国运载火箭技术研究院, 北京 100076;
4. 航天材料及工艺研究所, 北京 100076;
5. 中南大学 材料科学与工程学院, 长沙 410083

摘 要: 研究厚度为 20 mm 的 2A55 铝锂合金板 T6 态时效(165 °C, 24 h)后的力学性能及晶粒组织。以 20 mm 厚度板材为原料, 旋压制备直径为 1 m 的 2A55 铝锂合金旋压壳体, 研究旋压壳体相同 T6 态时效后的时效析出相、晶粒组织及沿壳体轴向和周向的力学性能分布。结果表明, 旋压壳体 T6 态时效后的析出相包括大量 T1 相 (Al₂CuLi)、部分 δ'相 (Al₃Li) 和 θ相 (Al₂Cu)。T1 相分布不均匀, 亚晶界分布密集, 但沿大角度晶界形成沿晶无沉淀带。板材同一方向力学性能基本一致, 但不同方向存在各向异性, 沿轧制方向强度最高而沿 45°方向强度最低。旋压过程导致壳体不同位置周向和轴向与原始轧制方向的夹角变化, 晶粒长宽比和织构不同。相应地, 旋压壳体沿相同周向或轴向的力学性能分布存在很大差异。原始板材的各向异性在旋压壳体晶粒组织及力学性能分布方面存在遗传效应。

关键词: 铝锂合金; 旋压成型; 各向异性; 力学性能; 织构

(Edited by Wei-ping CHEN)